PNAS RESEARCH ARTICLE | EARTH, ATMOSPHERIC, AND PLANETARY SCIENCES

Observed rapid adjustment of the atmospheric boundary layer to submesoscale sea surface temperature fronts

Igor Uchoa[a,1], Jacob O. Wenegrat[a], Alex Kinsella[b], Inés M. Leyba[c], Larry W. O'Neill[c], and Luc Lenain[d]

Edited by Richard Rotunno, National Center for Atmospheric Research, Boulder, CO; received February 17, 2026; accepted June 5, 2026

Current understanding of the role of ocean variability in air–sea exchange is constrained to large and mesoscale dynamics. Oceanic fronts and filaments with horizontal spatial scales of order 0.1 to 10 km—denoted submesoscale—are challenging to observe due to their fast-evolving flow and small spatiotemporal scales of variability. Observations investigating the air–sea fluxes at the submesoscale have shown substantial fluxes of heat, moisture, and momentum, affecting the structure of the overlying atmosphere. Here, modulations of the turbulent atmospheric boundary layer driven by ocean temperature anomalies are investigated using submesoscale-resolving ship and airborne measurements, providing in situ evidence of the atmospheric response to ocean submesoscale temperature variability. Observations suggest near-surface turbulent mixing driven by strong air–sea fluxes of heat and momentum, modifying the vertical structure of the planetary boundary layer. Linear regression coefficients between wind speed and sea surface temperature anomalies reveal a response similar in magnitude to that seen at larger scales, with an integrated change of 0.23 m s^{-1} °C^{-1}, but occurring over smaller length-scales, implying sharper gradients. Lagged correlations and scaling analysis imply a combined influence of horizontal advection and vertical turbulent mixing of momentum in the atmosphere, previously only described by numerical simulations. Observed cross-frontal wind divergences over the lower 200 m suggest coherent circulations with vertical velocities of order 1 cm s^{-1}. These observations confirm the rapid adjustment of the marine boundary layer to submesoscale ocean temperature variability and the importance of submesoscale-driven air–sea fluxes in changing the properties of the lower atmosphere, processes not resolved in most forecasting and prediction models.

air–sea interaction | submesoscale | planetary boundary layer | ocean mixed-layer | thermal feedback

The atmosphere and ocean interact dynamically via boundary fluxes of momentum and buoyancy. The variability of these fluxes is dictated in part by the dynamical scales of both fluids (1). The ocean is subject to changes in temperature and currents driven by atmospheric forcing at large scales (>1,000 km); whereas, at the oceanic mesoscale, sea surface temperature (SST) and current variability play a crucial role in transferring heat and momentum to and from the atmosphere (2). Recently, there has been an increased effort to understand air–sea interaction at smaller transitional regimes in the ocean such as the submesoscale (with horizontal length scales in the mid-latitudes of order 0.1 to 10 km). Processes at these scales are in a unique dynamical regime between meso- and turbulent scales in the ocean, and span across the micro- to mesoscale transition in the atmosphere (3). They are characterized by fast-evolving flows (with representative timescales near the inertial period) and strong density gradients associated with large vertical velocities that affect the vertical exchange of heat and nutrients in the ocean (4, 5). Observational evidence indicates that submesoscale ocean variability strongly affects surface fluxes of momentum, heat, and moisture (6–8), which are known to modify the marine atmospheric boundary layer (MABL) as well as the overlying troposphere, affecting, for example, precipitation, cloud coverage, and storm tracks (2, 9). These suggest pathways for air–sea coupling that are not adequately represented in typical low-resolution global models (10–13).

An important component of submesoscale air–sea interaction is the feedback mechanisms driven by sea surface temperature spatial variability, generally referred to as the thermal feedback. At the submesoscale, heat fluxes forced by SST anomalies alter surface winds (14–16), enhance potential energy fluxes (16, 17), and modify convective precipitation over boundary currents (13). Thermal feedbacks also introduce small-scale gradients in surface winds, which are associated with vertical velocities in the atmosphere (e.g., wind divergence, 18) or in the ocean (e.g., wind stress curl, 19) depending on the

Significance

Exchanges between the ocean and the atmosphere vary across spatial and temporal scales. Understanding the role of small oceanic fronts and filaments—classified as submesoscale—in air–sea fluxes remains limited due to the challenges inherent in measuring and resolving these features. This work provides observational evidence that submesoscale features actively modify the lower atmosphere through strong surface temperature gradients. This thermal response homogenizes the near-surface layer, altering near-surface winds and inducing vertical circulations that collectively modify atmospheric properties. These observations underscore the need to reassess how air–sea fluxes at submesoscale are represented in forecast and global climate models.

Author affiliations: [a]Department of Oceanic and Atmospheric Science, University of Maryland, College Park, MD 20742; [b]Department of Physical Oceanography, Woods Hole Oceanographic Institution, Woods Hole, MA 02543; [c]College of Earth, Ocean, and Atmospheric Sciences, Oregon State University, Corvallis, OR 02543; and [d]Scripps Institution of Oceanography, University of California, San Diego, La Jolla, CA 92037

Author contributions: I.U., J.O.W., A.K., I.M.L., L.W.O., and L.L. designed research; I.U., J.O.W., A.K., I.M.L., L.W.O., and L.L. performed research; I.U. analyzed data; and I.U., J.O.W., A.K., I.M.L., L.W.O., and L.L. wrote the paper.

The authors declare no competing interest.

This article is a PNAS Direct Submission.

Copyright © 2026 the Author(s). Published by PNAS. This article is distributed under Creative Commons Attribution-NonCommercial-NoDerivatives License 4.0 (CC BY-NC-ND).

[1]To whom correspondence may be addressed. Email: iufarias@umd.edu.

This article contains supporting information online at https://www.pnas.org/lookup/suppl/doi:10.1073/pnas.2605662123/-/DCSupplemental.

Published July 21, 2026.

Downloaded from https://www.pnas.org by UNIVERSITY OF MARYLAND; MCKELDIN LIBRARY on July 21, 2026 from IP address 129.2.179.140.

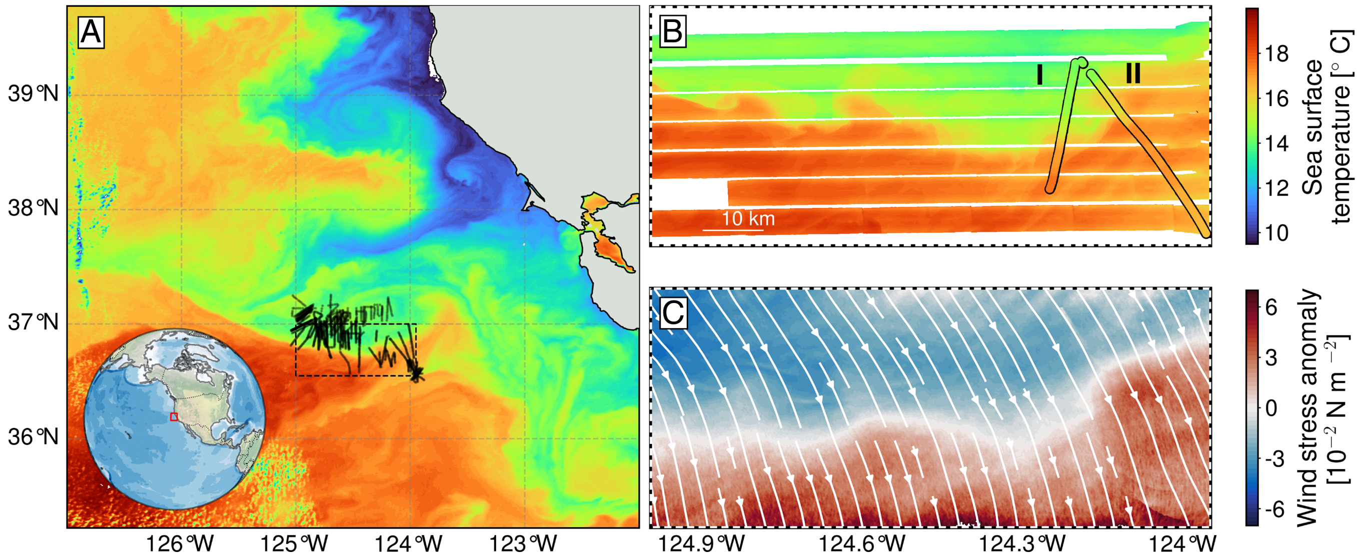

Fig. 1. Overview of the research mission. (*A*) Panoramic view of the SST distribution in the region on October 24, 2022, from Sentinel-3. The black scatter illustrates the sections measured with shipborne data during the mission (October 10–October 29, 2022), and the dashed box represents the subsections highlighted in the *Right* panels. (*B*) SST field at ~10 m resolution from the airborne measurements (MOSES) and in situ measurements of temperature by a towed conductivity-temperature-depth in the time span of 8 h (10 km spatial reference on the map). Sea surface temperature measurements were intercalibrated based on the in situ measurements included in sections I and II highlighted. (*C*) Spatial anomaly of wind stress magnitude in the same region overlaid with the wind streamlines. Outputs of wind stress and 10-m winds are from DopplerScatt at 200 m resolution.

Downloaded from https://www.pnas.org by UNIVERSITY OF MARYLAND; MCKELDIN LIBRARY on July 21, 2026 from IP address 129.2.179.140.

front-wind orientation (9), but these mechanisms have not been completely described at the submesoscale (11, 20). Although a body of work has explored the impact of the thermal feedbacks at the submesoscale using numerical experiments, observational studies of thermal coupling at the submesoscale—particularly those that resolve the vertical structure of the MABL response—remain scarce due to the challenges inherent in capturing fast-time and small-spatial scale processes (12, 21, 22).

Both large eddy simulations and regional numerical models indicate that changes in the turbulent mixing of momentum are the dominant factor altering surface winds in response to SST variations at the submesoscale (10, 11, 20, 23). In this mechanism, positive SST anomalies are associated with positive surface vertical heat flux anomalies which favor convective instability in the air column, generating turbulent mixing of momentum downward from aloft and accelerating surface winds (10). Conversely, negative SST anomalies generate a stratified internal boundary layer (IBL), suppressing mixing and decelerating surface winds (9, 24). This response differs dynamically from that at the larger mesoscale, where thermally induced pressure variations are also a key driver (18, 25). While prior work has observed aspects of air–sea coupling at submesoscale fronts, few coincident observations of both the horizontal ocean variability and vertical structure of MABL exist, making it difficult to compare with theoretical and numerical studies.

Here we utilize a unique combination of in situ and airborne remote sensing observations to describe how submesoscale SST variability drives changes in the wind and its associated MABL structure (Fig. 1). The observations were collected as part of a recent research campaign to observe submesoscale dynamics in the California Current System (26). The impacts of SST-driven submesoscale anomalies on the lower atmospheric structure are examined using high-frequency observations from shipborne LIDAR measurements, radiosondes and hydrographic profiles, and airborne remote sensing of surface temperature, winds, and currents. These observations provide detailed evidence of the role of submesoscale SST variability in driving turbulent mixing, changing boundary-layer stability, and generating vertical velocities in the lower atmosphere. Examination of the downwind spatial evolution of the MABL as the flow crosses sharp submesoscale fronts highlights the important joint roles of advection and turbulent mixing in determining the strength and location of the response. Together, these observations show the rapid adjustment of the MABL to submesoscale variability, and provide a validation of ocean–atmosphere feedback mechanisms inferred from high-resolution models (10, 11, 23).

Materials and Methods

The *Sub-Mesoscale Ocean Dynamics Experiment* (S-MODE) was a multi-instrument, multiplatform research effort measuring submesoscale dynamics and their associated air–sea interaction and vertical transport offshore of California (26). The 63 transects analyzed in this work were surveyed in the first intensive operational period of the mission (Fig. 1*A*), which occurred from October 7 to November 2, 2022. Conditions during this period were characterized by moderate (5 to 15 m s^{-1}) northwest winds, and a strong coastal upwelling front evident in orbital and suborbital SST imagery (Fig. 1, with larger-scale conditions discussed in *SI Appendix*). An exception to this was during a synoptic cold-front passage between October 16–19, associated with southerly winds and increased boundary-layer stability (*SI Appendix*, Fig. S2).

For surface measurements, a shipboard meteorological station at ~10 m height above the surface measured near-surface winds, air temperature, relative humidity, and shortwave and longwave radiation at approximately 1-min frequency. In addition, a towed conductivity-temperature-depth instrument (27) measured temperature in the upper 100 m of the ocean at a 3-min averaged sampling frequency (equivalent to an approximately 600 m average horizontal spacing between observations given the average ship speed). Latent and sensible heat flux components were calculated from these observations using the COARE 3.5 bulk flux algorithm (28) and net radiative heat flux was computed from the shipboard shortwave and longwave radiation measurements. It is relevant to note that bulk formula based algorithms such as COARE 3.5 are designed for larger scales, and the application in regions of strong spatial inhomogeneity is a source of uncertainty (3, 6). For the atmospheric vertical structure, frequent radiosonde soundings were conducted measuring winds, air-temperature, and relative

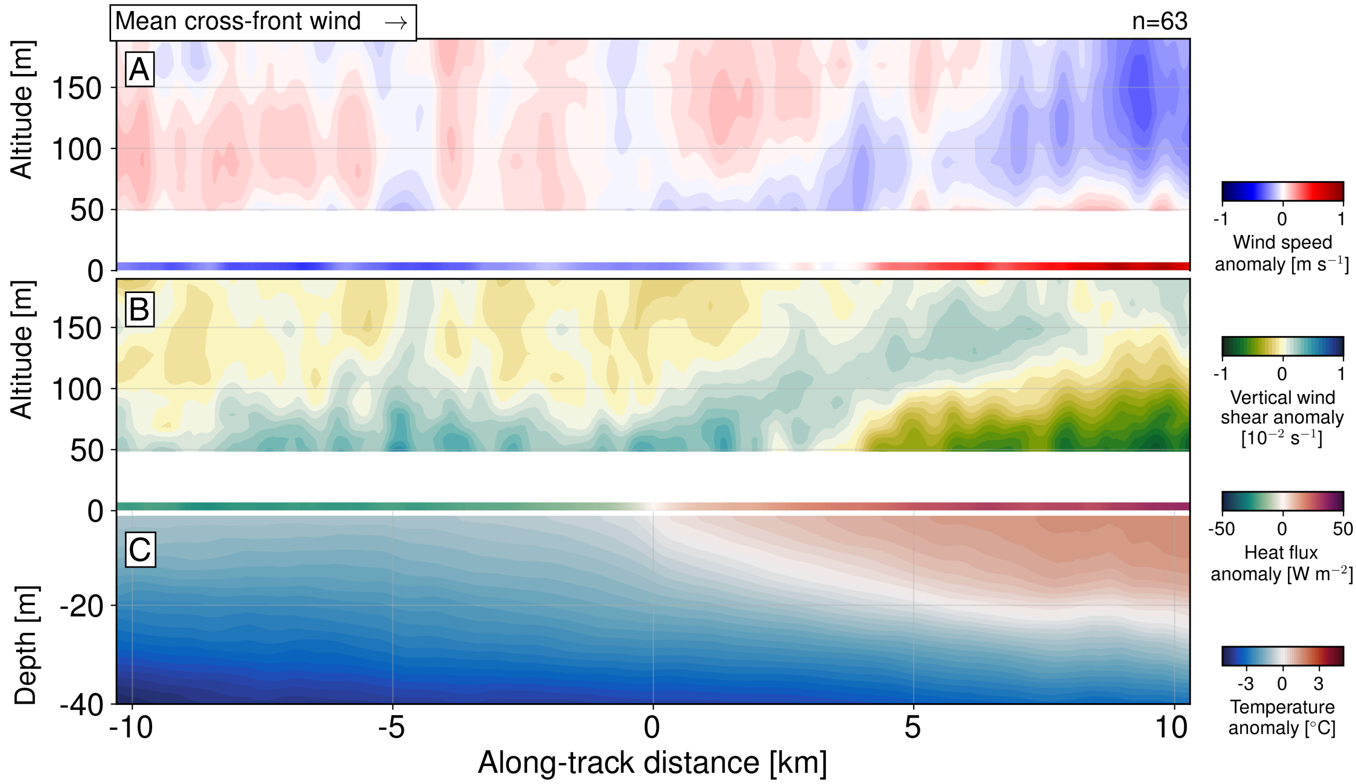

Fig. 2. Composites of atmospheric properties show a robust change in the near-surface atmosphere correlated to sea surface temperature variability. Averaged composites show spatial anomalies of (*A*) 10 m and 50 to 200 m in wind speed, (*B*) 50 to 200 m vertical wind shear and surface heat flux (color strip at 0 m), and (*C*) 2 to 40 m ocean temperature using the 63 cross-frontal sections of shipborne data. The spatial anomalies are computed by subtracting the along-track averages at every altitude for the atmosphere and at the surface for the ocean. Average across-front wind direction component (east-west) is depicted by the arrow symbol. A complementary figure showing the composite RMSD is available in *SI Appendix*, Fig. S5.

Downloaded from https://www.pnas.org by UNIVERSITY OF MARYLAND; MCKELDIN LIBRARY on July 21, 2026 from IP address 129.2.179.140.

humidity and binned to a 10-m vertical resolution (detailed information in *SI Appendix*). In addition, a shipborne upward-facing wind Doppler Lidar profiler (Vaisala WindCube) surveyed winds in the lower 200 m of the atmospheric boundary layer at 0.25 Hz, later averaged to 1-min sampling rate for consistency with the other atmospheric measurements. All velocity measurements from the Doppler profiler were corrected for the relative velocity of the ship. Airborne observations from a Ka-band Doppler scatterometer (DopplerScatt) (29, 30), measuring 10-m equivalent neutral vector winds at a horizontal resolution of 200 m, and the Multiscale Observing System of the Ocean Surface (MOSES) instrument (5), measuring SST at a horizontal resolution of approximately 5 m were also used in the analysis.

Results

Airborne and orbital SST imagery collected on October 24, 2022, depict a sharp, approximately east-west-oriented upwelling front with frontal instabilities characteristic of submesoscale dynamics and typical of this region (Fig. 1*A*). The similarity of spatial distributions between SST and wind stress magnitude anomalies is highlighted (Fig. 1 *B* and *C*). The approximately 2 °C SST difference across the front is closely aligned with spatial wind stress anomalies showing an approximately 6×10^{-2} N m^{-2} change, representing nearly 40% of the total spatially averaged wind stress magnitude in the region. These spatial correlations indicate significant differences in the air–sea momentum flux across the cold and warm sectors of the front, which we show below is a response to kilometer-scale SST gradients.

A composite mean of 63 shipboard transects across fronts and filaments associated with the upwelling front reveals the coupled ocean–atmosphere boundary-layer responses in subsurface temperature, surface heat fluxes, wind speed (WS), and vertical wind shear (VWS) (Fig. 2). Here, anomalies are defined by subtracting the along-track average of each section at every altitude for the atmosphere and the SST along-track average for the ocean. All ship transects were interpolated into an along-section coordinate system defined such that 0-km distance marks the location of the maximum SST gradient of each section, and then averaged together. The composite section highlights the close alignment between atmospheric and oceanic boundary layers. We find a shallow submesoscale mixed-layer front in the upper 20 m of the water column, associated with a strong horizontal SST gradient of ≈1 °C over a 10 km distance. The sharp changes of SST and the slow response of the near-surface air temperature generate heat flux anomalies on order of ±40 W m^{-2}, where sensible and latent heat components account for ≈30% and ≈50%, respectively (decomposition of outgoing heat flux components in the composite is shown in *SI Appendix*, Fig. S4).

In the atmosphere, the composite shows positive covariance between surface winds and SST (Fig. 2 *A* and *C*) in agreement with the expected thermal feedback mechanism (31, 32). A pronounced positive VWS anomaly that ascends downwind of the front suggests the development of an IBL in response to the SST change (at approximately 50 m height over the cold sector and 100 to 150 m over the warm sector, Fig. 2*B*). In the lower portion of the MABL (50 to 100 m), VWS anomalies of approximately $\pm 0.5 \times 10^{-2}$ s^{-1} are negatively correlated with surface SST and heat flux. This reduction in VWS is associated with reduced WS directly below the IBL top and increased WS near the surface (clearly seen in the 10-m

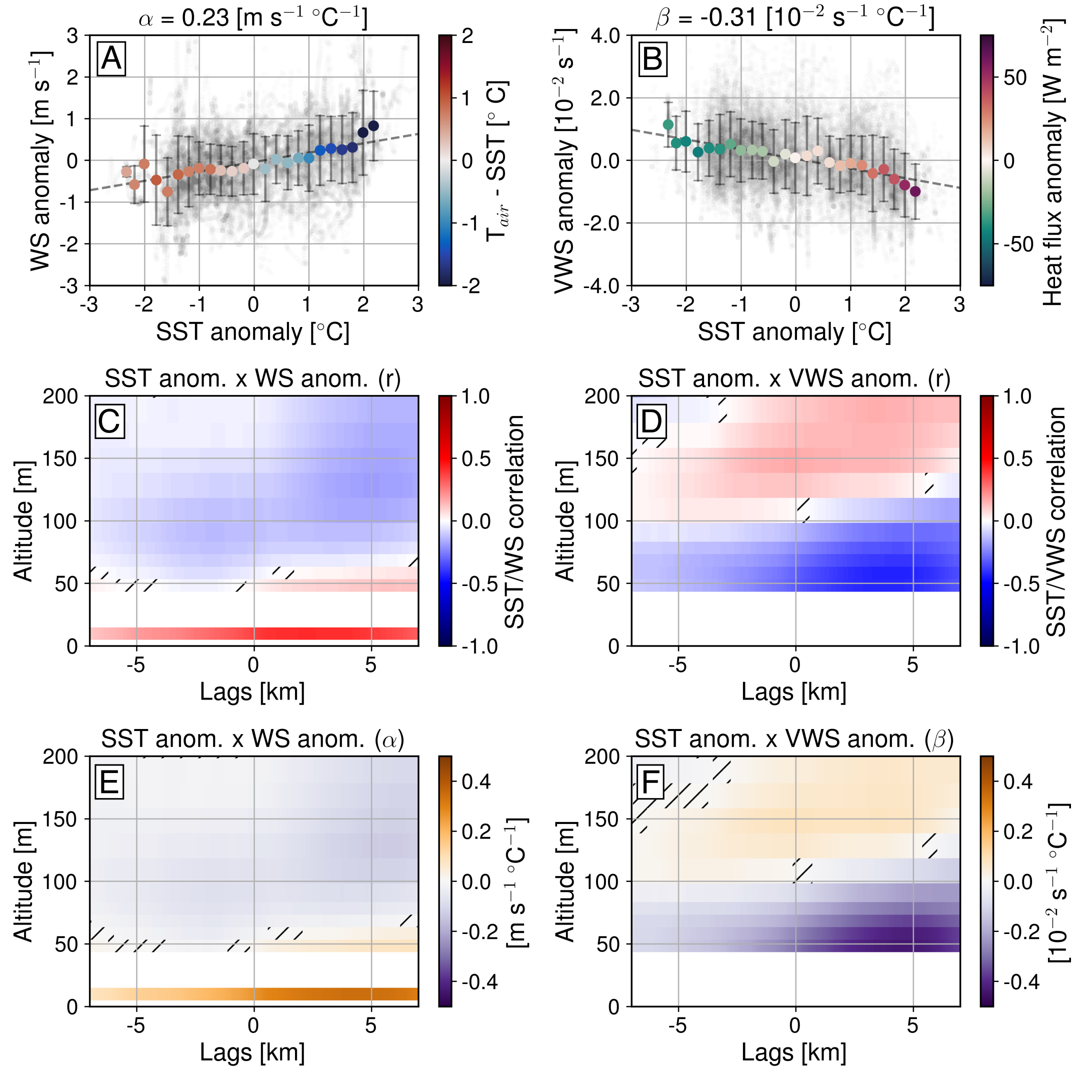

Fig. 3. Correlation (r) and coupling coefficient (α,β) analyses between SST and WS (*Left* column) and SST and VWS (*Right* column) using shipborne measurements of all available transects. (*A*) SST-binned scatterplots for 10-m wind speed and its coupling coefficient with markers colored according to their mean air–sea temperature difference. (*B*) SST-binned scatterplots for VWS at 50 m with colored markers representing surface net heat flux anomalies. Gray sample points plotted show the available data before binning. (*C*–*F*) Vertical variations of lagged correlations (*C* and *D*) and coupling coefficients (*E* and *F*) between SST and WS (*C* and *E*) and SST and VWS (*D* and *F*). The different lags correspond to a spatial displacement with respect to the SST front, namely, positive correlations for positive lags represent SST correlation with wind properties downstream of the front. The data analyzed are retrieved from all sections available in IOP1, with a 1-min running filter (equivalent to a 200 m spatial resolution), and interpolated onto an along-track frame of reference. Hashed regions represent values of regression coefficients that are not statistically different from zero based on a *P*-value greater than 0.05 from a two-sided *t* test.

shipboard measurements). This vertical inversion pattern in the WS anomaly is consistent with turbulent mixing of momentum (generated by warming from the surface) homogenizing the near-surface wind profile, decreasing the VWS in the turbulent boundary layer, and accelerating surface winds. This observed inversion of WS anomaly has previously only been described in numerical studies (e.g., refs. 10 and 20).

The strength of the thermal feedback mechanism is often quantified by computing coupling coefficients, defined as the slope of a linear regression fit between SST and WS anomalies (14, 32–35). Fig. 3 *A* and *B* shows binned scatterplots of WS and VWS anomalies as functions of SST anomaly using the data from the interpolated sections previously described. The average WS coupling coefficient ($\alpha = 0.23$ m s^{-1} °C^{-1}) is similar to satellite-based and buoy-derived observations at the mesoscale in mid-latitude regions (e.g., refs. 32 and 36). The agreement between WS and SST anomalies also aligns with the air–sea temperature difference (colored scatters in Fig. 3*A*). A further assessment of the thermal feedback, enabled here by the resolved vertical profiles of wind in the MABL, is to calculate a VWS anomaly coupling coefficient (β). The 50 m value of -0.31×10^{-2} s^{-1} °C^{-1} indicates the efficiency of SST anomalies in modifying the vertical structure of the near-surface wind profile. Numerical studies show that turbulent mixing reduces VWS near-surface (e.g., ref. 10), but have not provided quantitative values of this process. The overall negative covariance between VWS and SST is also aligned with the surface net heat flux anomalies (depicted by the colored points in Fig. 3*B*), consistent with net heat flux anomalies driving turbulent mixing and homogenizing the near-surface velocity profile.

While the importance of horizontal momentum advection in the atmospheric response at the ocean mesoscale remains a topic of discussion (18, 37), the response at the submesoscale likely has a significant advective component (11, 20). Lagged correlations

Downloaded from https://www.pnas.org by UNIVERSITY OF MARYLAND; MCKELDIN LIBRARY on July 21, 2026 from IP address 129.2.179.140.

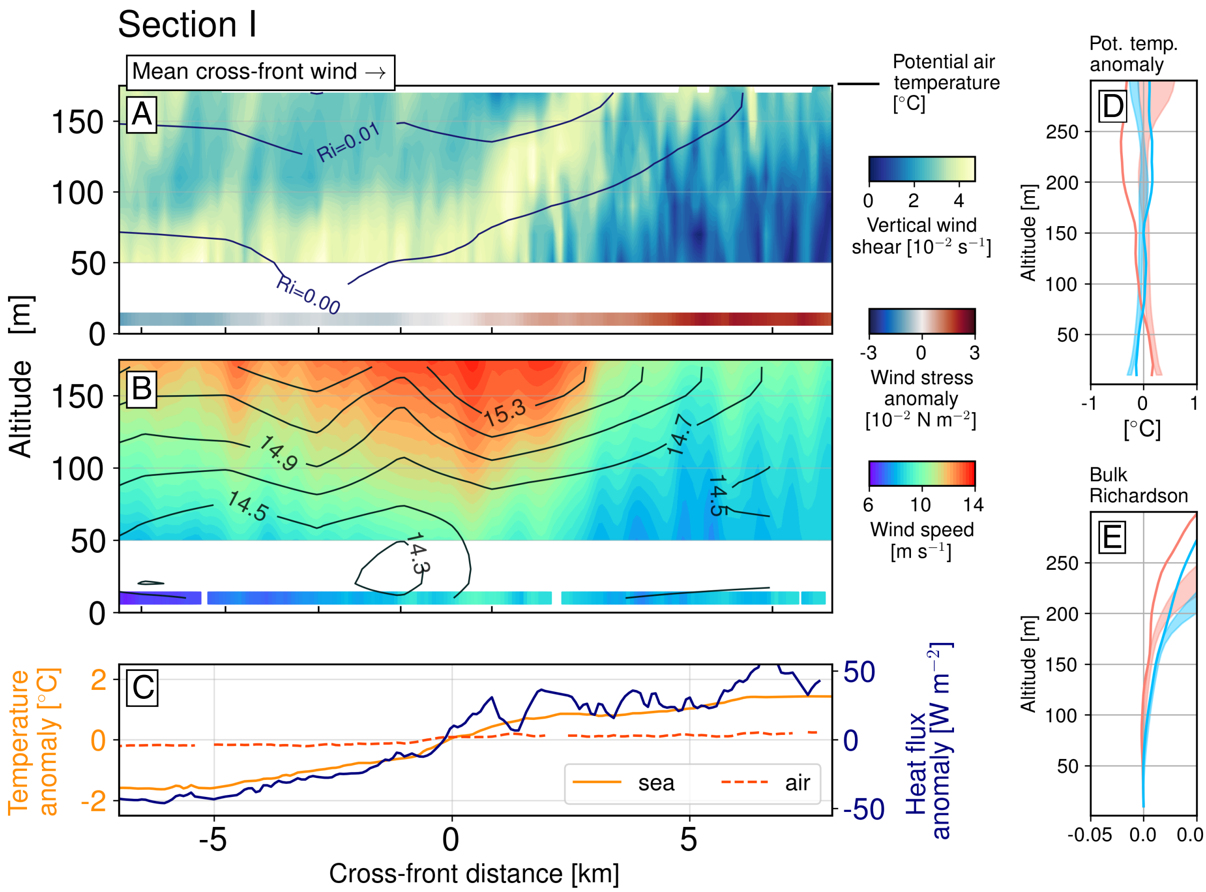

Fig. 4. Submesoscale temperature fronts imprint on the overlying atmosphere and modify the vertical structure of the air column. Measurements of the Section I transect (Fig. 1) of the mission. The cross-frontal distance is calculated by projecting the total distance of the section onto the approximated angle of the front derived from the SST image in Fig. 1*A*. (*A*) Wind stress anomaly from DopplerScatt at 10 m (shaded line), LIDAR vertical wind shear (color), and radiosonde bulk Richardson number (contours) from 10 to 175 m. (*B*) Wind speed (color) from the shipborne meteorological station and LIDAR measurements and radiosonde potential temperature (contours) along the submesoscale front from 10 to 175 m altitude. (*C*) Variability of the sea surface temperature, air temperature, and net heat flux anomalies calculated from the shipborne meteorological station. (*D* and *E*) Radiosonde profile composites parsed into cold (blue) and warm (red) profiles showing the vertical structure of potential temperature anomalies (*D*) and bulk Richardson number (*E*). Solid lines represent the average of profiles in Section I and shaded regions show the averaged profiles (and standard error of the mean) of the total samples used in the research mission.

between SST and WS (VWS) as a function of height shown in Fig. 3 *C* and *D* are computed by spatially displacing the SST anomalies from each transect to assess changes in correlation and regression coefficients. Although the total number of samples used for the lagged correlation analysis decreases as lag increases, it is sufficiently large to provide meaningful results of correlation and regression coefficient at $\approx\pm 7$ km lag as seen in Fig. 3 *C*–*F*. The lag correlations for WS are positive below 50 m, with a surface maximum at spatial lags of 2 to 4 km, indicating an atmospheric response downwind of the SST front. VWS also presents a similar pattern with enhanced negative correlations in the 50 to 75 m altitude range at spatial lags of 3 to 4 km. A sign change in the WS occurs around 75 m altitude (Fig. 3*D*), suggesting loss of momentum aloft of the turbulent boundary layer due to enhanced turbulent mixing of momentum downward as seen in Fig. 2. The altitude of the sign change in WS corresponds to the strong correlation values in VWS, delineating the height of the influence of turbulent mixing in the air column (Fig. 2*B*). Coupling coefficients in panels (*E* and *F*) show similar patterns with larger magnitude responses downstream of the front (i.e., 0.35 m s^{-1} °C^{-1} for WS and -0.4×10^{-2} s^{-1} °C^{-1} for VWS at 5 km lags) and an inversion of WS correlations at the region of high VWS, representative of the IBL limit.

The relative roles of horizontal advection and turbulent mixing in the lagged MABL wind adjustment observed here can be approximately scaled by assuming a vertical mixing timescale given by $\tau_m \sim H\Delta U/u^{*2}$ and an advective timescale of $\tau_a \sim L/U$ as in ref. 24, where u^* is the friction velocity, H the IBL height, L the cross-frontal length scale, U the wind speed, and ΔU is the change in wind speed across the front. Using values typical of the observations ($u^{*2} \approx 10^{-1}$ m^2 s^{-2}, $H \approx 10^2$ m, $L \approx 10^4$ m, $U \approx 10$ m s^{-1}, $\Delta U \approx 1$ m s^{-1}) the ratio of mixing to advective timescales is approximately unity, $\tau_m/\tau_a \sim 1$, with both on the order of $\tau_m, \tau_a \sim 10^3$ s. This underscores both the rapid adjustment of the lower MABL where the development of the shallow IBL allows a near-surface response to sharp submesoscale fronts, and limitations of classic conceptual models of the thermal feedback mechanism developed for larger spatial scales, which do not account for advection or the time needed to modulate convective turbulence after a frontal crossing. Thermally induced pressure adjustments at the submesoscale—which can generate pressure gradients and change the winds—were also investigated by estimating a pressure adjustment timescale given by $\tau_p \sim \rho_a L\Delta U/\Delta p$, where ρ_a is the air density and Δp the pressure difference across the front. Using the typical value of $\rho_a \approx 1$ kg m^{-3} and $\Delta p \approx 1$ Pa (estimated by observations as shown in *SI Appendix*, Fig. S4), we estimate that the pressure adjustment time scale is on the order of $\tau_p \sim 10^4$ s, which suggests a slower adjustment and smaller contribution of

Downloaded from https://www.pnas.org by UNIVERSITY OF MARYLAND; MCKELDIN LIBRARY on July 21, 2026 from IP address 129.2.179.140.

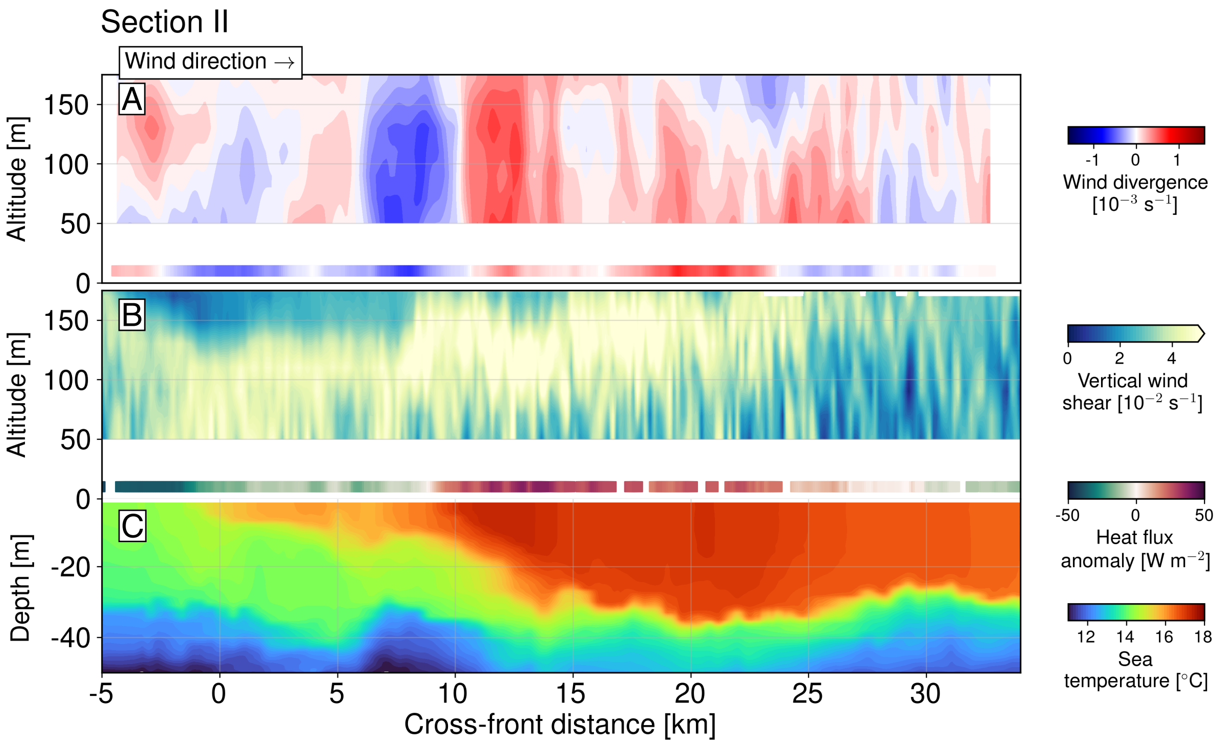

Fig. 5. Measurements of the Section II transect (Fig. 1*B*). (*A*) Total wind divergence from airborne scatterometry near-surface (10 m) from DopplerScatt fields and estimated divergence (i.e., along-transect gradient of the cross-frontal wind) at 50 to 175 m from LIDAR measurements. (*B*) Net surface heat flux anomaly and vertical wind shear from 50 to 175 m (LIDAR). (*C*) Ocean temperature from towed conductivity-temperature-depth measurements.

SST-induced pressure adjustment at the submesoscale as opposed to the mesoscale (18, 37).

Case Study Sections. To examine the MABL response to submesoscale fronts in greater detail, we focus on a specific case study from October 24, 2022 (sections labeled in Fig. 1*B*). These sections were selected based on a combination of factors: coincident sampling of the front by multiple instruments (including airborne sensors and radiosondes), favorable meteorological conditions (notably strong cross-front winds), and sufficient cross-front survey length. The SST and wind stress anomalies from airborne remote sensing are shown in Fig. 1 *B* and *C*, as previously discussed. Additional meteorological context is provided in *SI Appendix*.

Section I surveys an approximately 15 km transect across a submesoscale SST front with 7 radiosonde profiles (Fig. 4). Similar to the composite picture shown in Fig. 2, an air–sea temperature difference across the front, while small in an absolute sense, is associated with significant surface heat flux anomalies. Over the cold side of the front, the high VWS band and strong stratification delineate the IBL (Fig. 4 *A* and *B* for negative cross-front distances). In contrast, over the warm side of the front, the high VWS band is eroded through convection, leading to a growth of the resulting IBL height. Profiles of potential temperature also highlight the thermal response in the lower 75 m of the atmosphere showing an average difference across the front of ≈0.3 °C (Fig. 4*D*). Dynamically, these two boundary-layer regimes are supported by estimations of the bulk Richardson number (*Ri*) (Fig. 4 *B* and *E*, calculated as in ref. 38, and *SI Appendix*). The warming of the air column over the warm side of the front leads to more convectively unstable conditions ($Ri \lesssim 0$), whereas over the cold side of the front, the near-surface layer becomes unstable predominantly due to enhanced shear. A similar response of the boundary-layer structure and stability is also seen when composite averaging 74 soundings from 11 transects as a function of their location on the warm or cold side of the front (shaded areas in Fig. 4 *D* and *E*). Bulk Richardson number profile composites show that over the warm sector of the front the lower portion of the air column is less stable than over the cold sector, due to changes in both stratification and VWS (e.g. Figs. 2*B* and 4*A*).

Section II provides a longer transect (≈40 km) to examine the downwind evolution beyond what is captured by the shorter sections that focus on the frontal region (Fig. 1*B*). This section, taken approximately 1 h after Section I, crosses a warm filament with stronger cold-to-warm transitions (from 0 to 10 km) and a weaker warm-to-cold transition near 25 km (Fig. 5*C*). The region of lowest near-surface VWS values is found ≈5 km downstream of the warmest region of the filament (i.e., ≈20 km), consistent with the analysis in Fig. 3*D*. The elevated VWS layer, previously identified as marking the top of the developing IBL, grows in height with downwind distance at a rate of approximately 50 m height per 10 km horizontal distance, suggesting a Lagrangian rate of IBL deepening of approximately 5 cm s^{-1} (using $U \approx 10$ m s^{-1}).

The variations in WS across the front are associated with large horizontal divergences (Fig. 5*A*). Since the wind direction and ship transect are both aligned and approximately cross-frontal, the along-section gradient of the cross-front wind can be used as an estimate of divergence (Fig. 1). Cross-front wind divergence shows a strong dipole pattern around the region of warmest SST and sharp SST gradient (i.e., 10 km cross-section distance). A similar pattern of the surface horizontal divergence is found in the DopplerScatt measurements interpolated to the ship-track, despite an approximately 4-h lag between the observations (Fig. 5*A*). The divergence signal decays from the surface toward 200 m

Downloaded from https://www.pnas.org by UNIVERSITY OF MARYLAND; MCKELDIN LIBRARY on July 21, 2026 from IP address 129.2.179.140.

altitude (the upper extent of the LIDAR observations), suggesting vertical velocities of $\mathcal{O}(1 \text{ cm s}^{-1})$, consistent with ageostrophic circulations previously identified in idealized numerical studies (11, 20, 39). To what extent the presence of these coherent overturning circulations induced by submesoscale SST fronts modifies the transport of momentum or other properties through the boundary layer is still uncertain, however numerical evidence suggests their potential role in convective organization and diabatic heating of the lower atmosphere (11, 13, 40). Models or observations that do not resolve the $\mathcal{O}(1 \text{ km})$ scale submesoscale fronts will not represent these vertical circulations and associated impacts.

Summary

In this work, we present observations of the response of the MABL to submesoscale SST variability using unique high-resolution measurements of a submesoscale frontal region in the California Current System. Submesoscale SST variability is shown to drive surface fluxes of heat that reshape the properties and vertical structure of the lower atmosphere, ultimately feeding back onto the surface momentum flux. These estimates of heat and momentum fluxes, cross-front wind divergence, and thermal feedback coupling coefficients provide a description of the dynamics of the air–sea feedback processes occurring at the ocean submesoscale.

The observed correlations between horizontal near-surface winds and their vertical shear and SST anomalies together with the strong surface heat flux forcing from an air–sea temperature imbalance support the key role of downward momentum mixing at small spatial scales. In this mechanism, enhanced vertical heat fluxes drive turbulence that vertically redistributes momentum over the warm sectors of the front, consistent with the wind-speed anomaly pattern observed here (Fig. 2*A*). The presence of a thin IBL over the cold-sectors, and a gradient in IBL height across the SST front, are evident both in VWS and in cross-frontal changes in boundary-layer stability quantified by the bulk Richardson number calculated from radiosondes. Associated with these changes in boundary-layer structure is the presence of dipoles of horizontal divergence that extend from the surface to 200 m height (the vertical limit of our observations), implying vertical circulations driven by either surface buoyancy generation or differential near-surface horizontal winds (cf. 11, 20, 23). The extent to which these near-surface coherent structures modify vertical fluxes in the MABL is not currently established, however numerical results have implicated similar features in modifying cloud coverage, moisture, and precipitation (6, 12, 13).

The coupled evolution of the ocean and atmospheric boundary layer is further quantified by defining coupling coefficients between SST and WS/VWS as a function of height above surface and spatial lags. WS and VWS are both most strongly correlated to SST at spatial lags of approximately 3 km, which suggests an adjustment timescale of $\mathcal{O}(10^3 \text{ s})$, highlighting the likely joint influences of advection and turbulent mixing in the response, rather than horizontal pressure gradients as in the mesoscale. Coupling coefficients between SST and WS/VWS are also shown as a function of height, providing a measure of how surface anomalies are communicated vertically downwind of the frontal crossing. The observed thermally induced inversion of the WS anomaly (or increase of VWS) with height has previously been reported only in numerical simulations. Together, these results emphasize the importance of near-surface dynamics of the MABL in enabling a rapid atmospheric response to fronts whose horizontal scales are comparable to the synoptic planetary boundary-layer height, and provide metrics for evaluating the fidelity of numerical models that parameterize turbulent mixing.

Implications

While extensive previous work has documented the mechanisms and impact of mesoscale air–sea coupling, far less is known about these processes at the submesoscale. The observations presented here demonstrate that the MABL can adjust over very short length scales to sharp SST fronts, with a downstream development likely governed by the combined effects of horizontal advection and vertical mixing. Robust relationships linking SST anomalies to the downstream evolution in WS and VWS as a function of height provide a benchmark for validating high-resolution model representations of these coupled boundary-layer physics. At coarser horizontal and vertical resolutions, typical of weather forecasting or climate models, the submesoscale is largely unresolved, such that the adjustment of the MABL, modifications of heat and momentum fluxes, and subsequent feedbacks are absent or incorrectly represented. Small-scale variability has been shown to affect the large scale mean of the turbulent heat flux (41) and high-resolution numerical simulations imply upscaling effects in the energy reservoirs of the upper ocean driven by changes in the submesoscale SST variability (17). The degree of coupling of submesoscale variability and larger scales is still uncertain (3), but will likely be tied to the dynamical response of the boundary layer—and associated control of air–sea fluxes—as explored here. Emerging coupled ocean–atmosphere satellite missions and the continued development of high-resolution global coupled models, provide an opportunity to quantify the integrated impact of these submesoscale air–sea interaction mechanisms (42–44).

Data, Materials, and Software Availability. The shipborne and airborne observations used here are available for download from the Physical Oceanography Distributed Active Archive Center (PODAAC) (45–50).

ACKNOWLEDGMENTS. This work is a contribution to the S-MODE project an EVS-3 Investigation awarded under NASA Research Announcement NNH17ZDA001N-EVS3. I.U. and J.O.W. were supported by NASA grants 80NSSC21K0554 and 80NSSC24K0412 awarded under NASA Research Announcement NNH20ZDA001NPO to the University of Maryland, College Park. L.L. was supported by 80NSSC19K1688 and NSF OCE2219752. I.M.L. and L.W.O. were supported by NASA grant 80NSSC19K1011 to Oregon State University. A.K. was supported by NASA grant 80NSSC19K1256 to Woods Hole Oceanographic Institution.

1. S. P. Bishop, R. J. Small, F. O. Bryan, R. A. Tomas, Scale dependence of midlatitude air-sea interaction. *J. Clim.* **30**, 8207–8221 (2017).
2. H. Seo *et al*., Ocean mesoscale and frontal-scale Ocean-atmosphere interactions and influence on large-scale climate: A review. *J. Clim.* **36**, 1981–2013 (2023).
3. L. Nuijens *et al*., The air-sea interaction (ASI) submesoscale: Physics and impact. In *Lorentz workshop* (2024). https://doi.org/10.5065/78ac-qd31
4. Z. Su *et al*., High-frequency submesoscale motions enhance the upward vertical heat transport in the global ocean. *J. Geophys. Res. Oceans* **125**, e2020JC016544 (2020).
5. H. S. Torres *et al*., Submesoscale eddy contribution to ocean vertical heat flux diagnosed from airborne observations. *Geophys. Res. Lett.* **52**, e2024GL112278 (2025).
6. M. Shao *et al*., The variability of winds and fluxes observed near submesoscale fronts. *J. Geophys. Res. Oceans* **124**, 7756–7780 (2019).
7. S. Iyer, K. Drushka, E. J. Thompson, J. Thomson, Small-scale spatial variations of air-sea heat, moisture, and buoyancy fluxes in the tropical trade winds. *J. Geophys. Res. Oceans* **127**, e2022JC018972 (2022).
8. S. L. Castro, G. A. Wick, A. T. Jessup, Modulation of the ocean surface skin temperature and heat flux in the presence of strong SST fronts. *J. Geophys. Res. Oceans* **130**, e2025JC022713 (2025).

Downloaded from https://www.pnas.org by UNIVERSITY OF MARYLAND; MCKELDIN LIBRARY on July 21, 2026 from IP address 129.2.179.140.

9. R. J. Small *et al*., Air-sea interaction over ocean fronts and eddies. *Dyn. Atmos. Oceans* **45**, 274–319 (2008).
10. E. D. Skyllingstad, D. Vickers, L. Mahrt, R. Samelson, Effects of mesoscale sea-surface temperature fronts on the marine atmospheric boundary layer. *Bound. Layer Meteorol.* **123**, 219–237 (2007).
11. J. O. Wenegrat, R. S. Arthur, Response of the atmospheric boundary layer to submesoscale sea surface temperature fronts. *Geophys. Res. Lett.* **45**, 13505–13512 (2018).
12. H. Yang *et al*., Observations reveal intense air-sea exchanges over submesoscale ocean front. *Geophys. Res. Lett.* **51**, e2023GL106840 (2024).
13. F. Vivant *et al*., Ocean submesoscale fronts induce diabatic heating and convective precipitation within storms. *Commun. Earth Environ.* **6**, 69 (2025).
14. C. Conejero, L. Renault, F. Desbiolles, J. McWilliams, H. Giordani, Near-surface atmospheric response to meso-and submesoscale current and thermal feedbacks. *J. Phys. Oceanogr.* **54**, 823–848 (2024).
15. Y. Bai *et al*., Sub-mesoscale wind-front interactions: The combined impact of thermal and current feedback. *Geophys. Res. Lett.* **50**, e2023GL104807 (2023).
16. L. Renault *et al*., Unraveling the impacts of submesoscale thermal and current feedbacks on the low-level winds and oceanic submesoscale currents. *J. Phys. Oceanogr.* **54**, 2463–2486 (2024).
17. I. Uchoa, J. Wenegrat, L. Renault, Sink of eddy energy by submesoscale sea surface temperature variability in a coupled regional model. *J. Phys. Oceanogr.* **55**, 993–1007 (2025).
18. S. Minobe, A. Kuwano-Yoshida, N. Komori, S. P. Xie, R. J. Small, Influence of the Gulf Stream on the troposphere. *Nature* **452**, 206–209 (2008).
19. P. Gaube, D. B. Chelton, R. M. Samelson, M. G. Schlax, L. W. O'Neill, Satellite observations of mesoscale eddy-induced Ekman pumping. *J. Phys. Oceanogr.* **45**, 104–132 (2015).
20. H. Jacquet, A. Ayet, F. Couvreux, Atmosphere response to an oceanic submesoscale SST front: A coherent structure analysis. *J. Geophys. Res. Atmos.* **130**, e2024JD042312 (2025).
21. C. Friehe *et al*., Air-sea fluxes and surface layer turbulence around a sea surface temperature front. *J. Geophys. Res. Oceans* **96**, 8593–8609 (1991).
22. L. Mahrt, D. Vickers, E. Moore, Flow adjustments across sea-surface temperature changes. *Bound. Layer Meteorol.* **111**, 553–564 (2004).
23. P. P. Sullivan, J. C. McWilliams, J. C. Weil, E. G. Patton, H. J. Fernando, Marine boundary layers above heterogeneous SST: Across-front winds. *J. Atmos. Sci.* **77**, 4251–4275 (2020).
24. R. M. Samelson *et al*., On the coupling of wind stress and sea surface temperature. *J. Clim.* **19**, 1557–1566 (2006).
25. N. Schneider, B. Qiu, The atmospheric response to weak sea surface temperature fronts. *J. Atmos. Sci.* **72**, 3356–3377 (2015).
26. J. T. Farrar *et al*., S-MODE: The sub-mesoscale ocean dynamics experiment. *Bull. Am. Meteorol. Soc.* **106**, E657–E677 (2025).
27. M. Dever *et al*., EcoCTD for profiling oceanic physical-biological properties from an underway ship. *J. Atmos. Oceanic Tech.* **37**, 825–840 (2020).
28. J. B. Edson *et al*., On the exchange of momentum over the open ocean. *J. Phys. Oceanogr.* **43**, 1589–1610 (2013).
29. A. Wineteer, H. S. Torres, E. Rodriguez, On the surface current measurement capabilities of spaceborne Doppler scatterometry. *Geophys. Res. Lett.* **47**, e2020GL090116 (2020).
30. A. Wineteer *et al*., Exploring the characteristics of ocean surface winds at high resolution with Doppler scatterometry. *Geophys. Res. Lett.* **51**, e2024GL113455 (2024).
31. D. B. Chelton, S. P. Xie, Coupled ocean-atmosphere interaction at oceanic mesoscales. *Oceanography* **23**, 54–69 (2010).
32. L. W. O'Neill, D. B. Chelton, S. K. Esbensen, Covariability of surface wind and stress responses to sea surface temperature fronts. *J. Clim.* **25**, 5916–5942 (2012).
33. S. Moreton, D. Ferreira, M. Roberts, H. Hewitt, Air-sea turbulent heat flux feedback over mesoscale eddies. *Geophys. Res. Lett.* **48**, e2021GL095407 (2021).
34. F. Desbiolles, M. Alberti, M. E. Hamouda, A. N. Meroni, C. Pasquero, Links between sea surface temperature structures, clouds and rainfall: Study case of the mediterranean sea. *Geophys. Res. Lett.* **48**, e2020GL091839 (2021).
35. L. Renault, C. Conejero, J. Wenegrat, I. Uchoa, Interplay of submesoscale current and thermal feedbacks: A seasonal perspective in the Gulf Stream. *Geophys. Res. Lett.* **52**, e2025GL116960 (2025).
36. L. W. O'Neill, Wind speed and stability effects on coupling between surface wind stress and SST observed from buoys and satellite. *J. Clim.* **25**, 1544–1569 (2012).
37. L. W. O'Neill, S. K. Esbensen, N. Thum, R. M. Samelson, D. B. Chelton, Dynamical analysis of the boundary layer and surface wind responses to mesoscale SST perturbations. *J. Clim.* **23**, 559–581 (2010).
38. Y. Zhang *et al*., On the computation of planetary boundary-layer height using the bulk Richardson number method. *Geosci. Model Dev.* **7**, 2599–2611 (2014).
39. P. P. Sullivan, J. C. McWilliams, J. C. Weil, E. G. Patton, H. J. Fernando, Marine boundary layers above heterogeneous SST: Alongfront winds. *J. Atmos. Sci.* **78**, 3297–3315 (2021).
40. X. Chen *et al*., Impacts of weak sea surface temperature warm anomalies on local trade cumulus cloudiness in large eddy simulations. *J. Adv. Model. Earth Syst.* **17**, e2024MS004778 (2025).
41. J. J. Busecke *et al*., The impact of sub-grid heterogeneity on air-sea turbulent heat flux in coupled climate models. *Geophys. Res. Lett.* **52**, e2025GL114951 (2025).
42. P. López-Dekker *et al*., "Harmony: an Earth explorer 10 mission candidate to observe land, ice, and ocean surface dynamics" in *IGARSS 2019-2019 IEEE International Geoscience and Remote Sensing Symposium* (IEEE, Yokohama, Japan, 2019), pp. 8381–8384, 10.1109/IGARSS.2019.8897983.
43. B. Stevens *et al*., DYAMOND: The dynamics of the atmospheric general circulation modeled on non-hydrostatic domains. *Prog. Earth Planet. Sci.* **6**, 1–17 (2019).
44. M. Larrañaga *et al*., Assessing the future ODYSEA satellite mission for the estimation of ocean surface currents, wind stress, energy fluxes, and the mechanical coupling between the ocean and the atmosphere. *Remote Sens.* **17**, 302 (2025).
45. S-MODE Team, S-MODE L2 shipboard meteorological data from rawinsondes version 1 (2022). https://earthdata.nasa.gov/data/catalog/pocloud-smode-l2-shipboard-radiosondes-meteorology-v1-1. Accessed 28 April 2026.
46. S-MODE, SMODE shipboard WindCube LiDAR observations version 1 (2024). https://earthdata.nasa.gov/data/catalog/pocloud-smode-l2-shipboard-windcube-lidar-v1-1. Accessed 28 April 2026.
47. S-MODE Team, S-MODE shipboard uCTD and EcoCTD measurements version 1 (2022). https://earthdata.nasa.gov/data/catalog/pocloud-smode-l2-shipboard-uctd-ecoctd-v1-1. Accessed 28 April 2026.
48. E. Rodriguez *et al*., S-MODE DopplerScatt Level 2 Ocean Winds and Currents Version 2 (2023). https://earthdata.nasa.gov/data/catalog/pocloud-smode-l2-dopplerscatt-winds-current-v2-2. Accessed 28 April 2026.
49. J. Molemaker, S-MODE MOSES Level, 2 atmospherically-corrected sea surface temperature version 1 (2022). https://earthdata.nasa.gov/data/catalog/pocloud-smode-l2-moses-lwir-sst-v1-1. Accessed 28 April 2026.
50. S-MODE Team, S-MODE L2 shipboard thermosalinograph, meteorology, and bio-optics measurements version 1 (2022). https://earthdata.nasa.gov/data/catalog/pocloud-smode-l2-shipboard-tsg-v1-1. Accessed 28 April 2026.

Downloaded from https://www.pnas.org by UNIVERSITY OF MARYLAND; MCKELDIN LIBRARY on July 21, 2026 from IP address 129.2.179.140.